Supporting Information

Engineering CuO-HfO_2 interface toward enhanced electrochemical CO_2 reduction to C_2H_4

Xin Li,[a] *Lifen Li,*[b] *Lijun Wang,*[a] *Qineng Xia,*[b] *Leiduan Hao,*[a] *Xinyu Zhan,*[a] *Alex W. Robertson*[c] *and Zhenyu Sun**[a]

[a] State Key Laboratory of Organic-Inorganic Composites, College of Chemical Engineering, Beijing University of Chemical Technology, Beijing 100029, P. R. China

[b] College of Biological, Chemical Science and Engineering, Jiaxing University, Jiaxing, Zhejiang 314001, P. R. China

[c] Department of Physics, University of Warwick, Coventry, UK

E-mail: sunzy@mail.buct.edu.cn

Experimental

Materials and reagents

All chemicals used in this work were of analytical grade and used as supplied. Copper(II) acetate monohydrate ($Cu(Ac)_2 \cdot H_2O$, product number: C108085), Hafnium chloride ($HfCl_4$, product number: C10851600), and sodium hydroxide (NaOH, product number: S111518) were purchased from Aladdin. Nafion solution (5 wt%) was supplied by Sigma-Aldrich. Nafion membranes were provided by Alfa Aesar. Ultrapure water (18.2 MΩ) was obtained from a Millipore system for preparing the sample solutions, electrolytes, and for washing. Carbon dioxide gas (99.999% purity) and argon gas (99.999% purity) were both provided by Beijing Haipu Gas Co., Ltd. KOH and $KHCO_3$ were obtained from Macklin.

Synthesis of CuO_x/HfO_2 catalysts

The CuO_x/HfO_2 catalyst was prepared by a hydrothermal method. NaOH was used as a precipitating agent. Typically, hydroxides were first precipitated by dropwise addition of NaOH solution into the aqueous mixture of $Cu(Ac)_2 \cdot H_2O$ and $HfCl_4$. After stirring for 60 min, the solution was transferred to a 100 mL Teflon-lined steel reactor and heated at 180 °C for 24 h, followed by natural cooling down to room temperature. Finally, the resulting solids were separated by centrifugation and washed with ultrapure water several times and then dried at 60 °C overnight. A series of CuO_x/HfO_2(a) composites were synthesized by using the same recipes except for the molar ratio of Cu and Hf (a denotes the Cu-to-Hf molar ratio, i.e., 2:1, 3:2, 1:1, 2:3, and 1:2).

Characterization

Powder X-ray diffraction (XRD) was recorded on the D/MAX−RC diffractometer operated at 30 kV and 100 mA with Cu Kα radiation (λ = 0.15418 nm) at a scanning rate of 5 ° min^{-1}. X-ray photoelectron spectroscopy (XPS) experiments were carried out using Thermo Scientific ESCALAB 250Xi instrument. The instrument was equipped with an electron flood and a scanning ion gun. All spectra were calibrated according to the C 1s binding energy at 284.8 eV. The binding energy was corrected for surface charging by taking the C 1s peak of contaminant carbon as a reference at 284.5 eV. Raman spectra were collected with a Renishaw in Via Raman microscope with an He/Ne Laser excitation at 532 nm (2.33 eV). In situ Raman measurements were obtained using a Renishaw in Via Raman microscope in a flow cell and a water immersion objective (63×) with a 532 nm laser. A spectroelectrochemical cell with Pt wire and Ag/AgCl electrode serving as the counter and the reference electrodes respectively were used for the in situ spectroelectrochemical measurements. Scanning electron microscopy (SEM) was made on the S-4800 microscope with a 3 kV accelerating voltage. Transmission electron microscopy (TEM) was conducted using a JEOL ARM200 microscope operated with 200 kV accelerating voltage. Hydrogen temperature-programmed reduction (H_2-TPR) experiments were conducted in a quartz tube reactor equipped with a thermal conductivity detector (TCD) using a Micromeritics AutoChem HP 2950 instrument. Before each measurement, the sample was first pre-treated in pure Ar at 200 °C for 30 min. Subsequently, a certain amount of the pre-treated sample was heated in a gas flow (50 cm^3 min^{-1}) of 10% H_2 in Ar from 50 to 750 °C at a ramp rate of 10 °C min^{-1}. Temperature programmed desorption of CO and CO_2 were carried out on an AutoChem 2920. CO_2 adsorption isotherms were measured on a NOVA 4000e Surface Area & Pore Size analyzer at 25 ºC. Before measurements, the sample was degassed at 120 ºC for 12 h. Electron spin resonance (ESR) spectroscopy was obtained at room temperature on a Bruker EMXPLUS10/12 spectrometer.

Cathode preparation

For H-type cell measurements, the working electrodes were prepared by loading catalysts suspension onto Toray Carbon fiber (CP) papers. Briefly, 1.2 mg of a catalyst was dispersed in 241.2 μL of a mixture of isopropanol (IPA), deionized water, and Nafion solution (5 wt%) with a corresponding volume ratio of 120: 120: 1.2 under bath ultrasonication for 30 min to form a homogeneous suspension. The suspension was then loaded onto a CP electrode with an area of 1.2 cm × 1.0 cm and dried under ambient conditions. For flow cell measurements, 2 mg of a catalyst and 2 μl of Nafion solution (5 wt%) were dispersed in 400 μl of IPA/H_2O mixture by ultrasonication to form a homogeneous ink. The ink was then deposited on a hydrophobic CP working electrode to form catalyst films with a catalyst loading of 1 mg cm^{-2}. For linear sweep voltammetry test in Ar- or CO_2-saturated 0.1 M $KHCO_3$ solution, 1 mg of a catalyst was dispersed in the mixture of 100 μL of ethanol, 100 μL of deionized water, and 100 μL of Nafion solution (1 wt%). Then the mixture was ultrasonicated for 30 min to form a homogeneous ink. 7.95 μL of the dispersion ink was then loaded onto glassy carbon electrode and dried under ambient conditions.

Electrochemical measurements

Linear sweep voltammetry test was performed in 0.1 M $KHCO_3$ solution using the CHI 760E (Shanghai CHI instruments Co., Ltd. China) electrochemical workstation with a scan rate of 2 mV s^{-1}. Ag/AgCl with saturated KCl solution was used as a reference electrode, Pt wire as a counter electrode, and glassy carbon as a working electrode. Rotating disk electrode (RDE) experiments were run on an AFMSRCE RDE control system (Pine Inc., USA). Before the experiment, the electrolyte solution in the working compartment was purged with Ar or CO_2 over 30 min to form a saturated solution. 1.0 mg of a catalyst was dispersed in a mixture solution of 100 μL ethanol, 100 μL deionized water, and 100 μL of Nafion solution (1 wt%). Then the mixture was subjected to bath ultrasonication for 30 min to form a homogeneous ink. 7.95 μL of the catalyst ink was then loaded onto glassy carbon electrode and dried under ambient conditions. The electrochemical impedance spectroscopy (EIS) experiments were operated in Ar-saturated 0.1 M $KHCO_3$ solution at an open circuit potential with frequencies from 10^6 Hz to 10 Hz.

The first set of controlled potential electrolysis of CO_2 was conducted in CO_2-saturated 0.1 M $KHCO_3$ electrolyte with an H-cell system separated by a Nafion 117 membrane at room temperature and atmospheric pressure. CO_2 was purged into the 0.1 M $KHCO_3$ solution for at least 30 min to remove residual air in the reservoir, then controlled potential electrolysis was performed at each potential for 60 min. Prior to ECR measurements, the Nafion membrane was pre-treated by heating in H_2O_2 solution (5%) and H_2SO_4 (0.5 M) at 80 °C for 1 h, respectively. Subsequently, the treated Nafion membrane was immersed in deionized water for 30 min and then washed with deionized water repeatedly. CPs with a size of 1.2 cm × 1 cm was used as working electrode. Pt wire and Ag/AgCl electrodes were applied as counter electrode and reference electrode, respectively. The CO reduction electrolysis was also performed in an H-cell system separated by an cation exchange membrane. Each compartment contained 10 ml of 0.1 M KOH electrolyte. The solution in the cathodic compartment was purged with CO for 20 min before the start of electrolysis.

Alternatively, electrocatalytic tests were carried out using an electrochemical flow cell consisting of a gas chamber, a cathodic chamber, and an anodic chamber. The working electrode was fixed between the gas chamber and the cathodic chamber, with the catalyst layer side facing the cathodic chamber. The cathode and anode compartments in the flow cell were separated by a anion exchange membrane. The Hg/HgO electrode and Pt foil were acted as the reference electrode and counter electrode, respectively. KOH was used as an electrolyte for both compartments. The catholyte was circulated using a peristaltic pump with a flow rate of 3 mL min^{-1}. CO_2 gas was supplied to the chamber located at the backside of the cathode at a flow rate of 20 mL min^{-1}.

The gaseous product from the cell was collected by the gas bag and analyzed using an Agilent 7890B gas chromatography system, which was equipped with two thermal conductivity detectors (TCD) and one flame ionization detector (FID) using helium as the internal standard. 20 mL of the produced gas in the dead volume of a gas bag (~ 2 L) was injected into the GC under identical conditions (e.g., pressure, temperature, and time) using a sample lock syringe. CO and H_2 mole fractions of injected samples were determined based on GC calibration curve. After each electrolysis, the collected liquid products such as formic acid was quantified by ^{1}H nuclear magnetic resonance (^{1}H NMR, Bruker 400 MHz) using a solvent pre-saturation technique to suppress the water peak.

All potentials in this study were measured against the Ag/AgCl reference electrode (in saturated KCl solution) and converted to the RHE reference scale by

$$E\ (vs.\ \mathrm{RHE}) = E\ (vs.\ \mathrm{Ag/AgCl}) + 0.197\ \mathrm{V} + 0.0591 \times \mathrm{pH} \qquad \text{(Eq. S1)}$$

Faradaic efficiency (FE) measurements

The FE of each product was calculated by $\mathrm{FE} = \frac{Z*n*F}{Q_{total}}$ (Eq. S2), where *Z* is the number of electrons transferred (Z = 2 for CO, HCOOH and H_2 production, 8 for CH_4 and 12 for C_2H_4), *n* the number of moles for a given product, *F* Faraday's constant (96485 C mol^{-1}), Q_{total} all the charge passed throughout the electrolysis process (measured by calculating the curve area of current density *vs.* time plot). CO and H_2 mole fractions of injected samples were calculated based on GC calibration curve. The production rate (PR) of a product was calculated by $\mathrm{PR} = \frac{I*FE}{Z*F}$ (Eq. S3), where *I* is the total current of all products. The cathodic energy efficiency (EE) for the ECR toward C_2H_4 is calculated using the following equation:

$$\mathrm{EE} = \mathrm{FE}_{C2H4} \times (E^0_{O2/H2O} - E^0_{CO2/C2H4}) / (E^0_{O2/H2O} - E^0_{CO2/C2H4} + \eta_{cathodic}) \qquad \text{(Eq. S4)}$$

where $E^0_{O2/H2O}$ is the thermodynamic equilibrium potential for the anode oxygen evolution reaction (i.e., 1.23 V *vs.* RHE), $E^0_{CO2/C2H4}$ is the thermodynamic equilibrium potential for the cathode CO_2 reduction reaction to form C_2H_4, and $\eta_{cathodic}$ is the overpotential for C_2H_4 formation.[1]

Number of active site measurements

In order to characterize the catalytic activities of CuO_x/HfO_2, CuO and HfO_2, the double layer capacitance (C_{dl}) was determined by measuring the capacitive current associated with double-layer charging from the scan-rate dependence of cyclic voltammetric stripping. A series of CV experiments at different scan rates (*e.g.*, 10, 20, 40, 60, 80, and 100 mV s^{-1}) were performed in 0.1 M $KHCO_3$ with saturated carbon dioxide to calculate the C_{dl} of each catalyst. All experiments were performed using the same surface area.

DFT calculation

All the DFT calculations are carried out within the periodic plane wave framework as implemented in the Vienna Ab Initio Simulation Package (VASP). The exchange-correlation potential is described by the generalized gradient approximation (GGA) with spin polarized Perdew–Burke–Ernzerhof (PBE) functional. The projector augmented wave (PAW) type pseudopotential is applied to describe the electron-ion interaction, and the plane-wave energy cutoff is set to 400 eV. All structures are optimized with a convergence criterion of 1×10^{-4} eV for the energy and 0.02 eV/Å for the forces. Brillouin zone sampling is employed using a Monkhorst-Packing grid with 3 × 3 × 1 for the calculated models.

We modeled the interface between CuO and HfO_2 by binding a HfO_2 cluster (Hf_8O_{16}) onto the Cu (111) slab (inset of Fig. 3h). The variation/trend of the Bader charges of the surface Cu atoms in the presence and absence of HfO_2 clusters was considered given that the Bader charge matches with the oxidation state qualitatively. It is assumed that the Bader charges of surface Cu atoms in Cu (111), Cu_2O (111), and CuO (111) correlate with the respective oxidation states of 0, +1, and +2. A linear relationship between the Bader charge and oxidation state (Fig. 3h) was acquired. The oxidation state of Cu atoms in CuO/HfO_2 can thus be derived from the correlation.

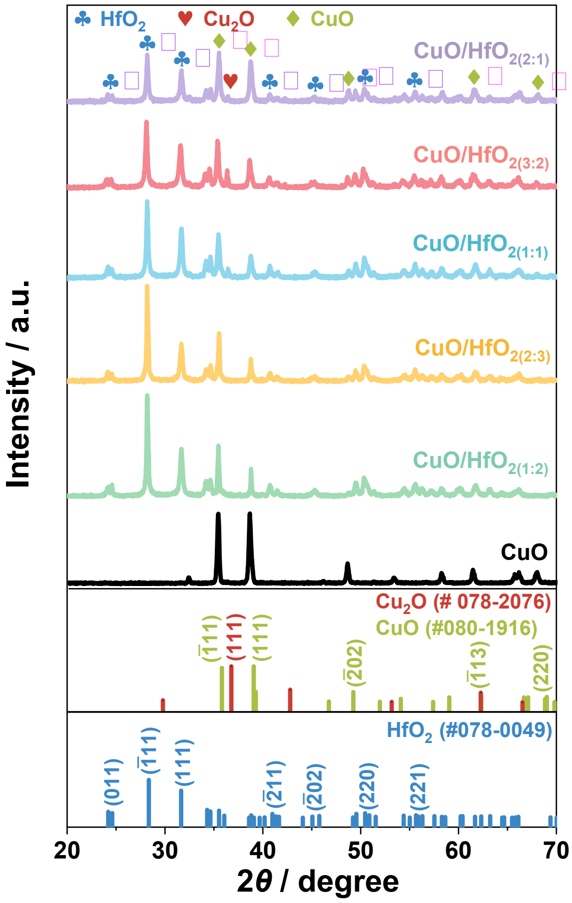

Fig. S1. XRD patterns of the as-obtained CuO, HfO$_2$, and CuO$_x$/HfO$_2$ with different Cu-to-Hf molar ratios.

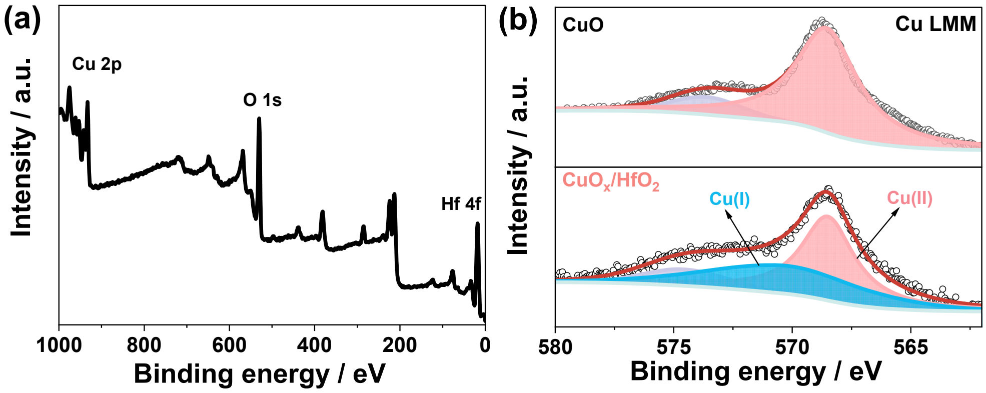

Fig. S2. (a) The wide-survey XPS spectrum of CuO$_x$/HfO$_2$(3:2). (b) Cu LMM spectra for CuO and CuO$_x$/HfO$_2$(3:2).

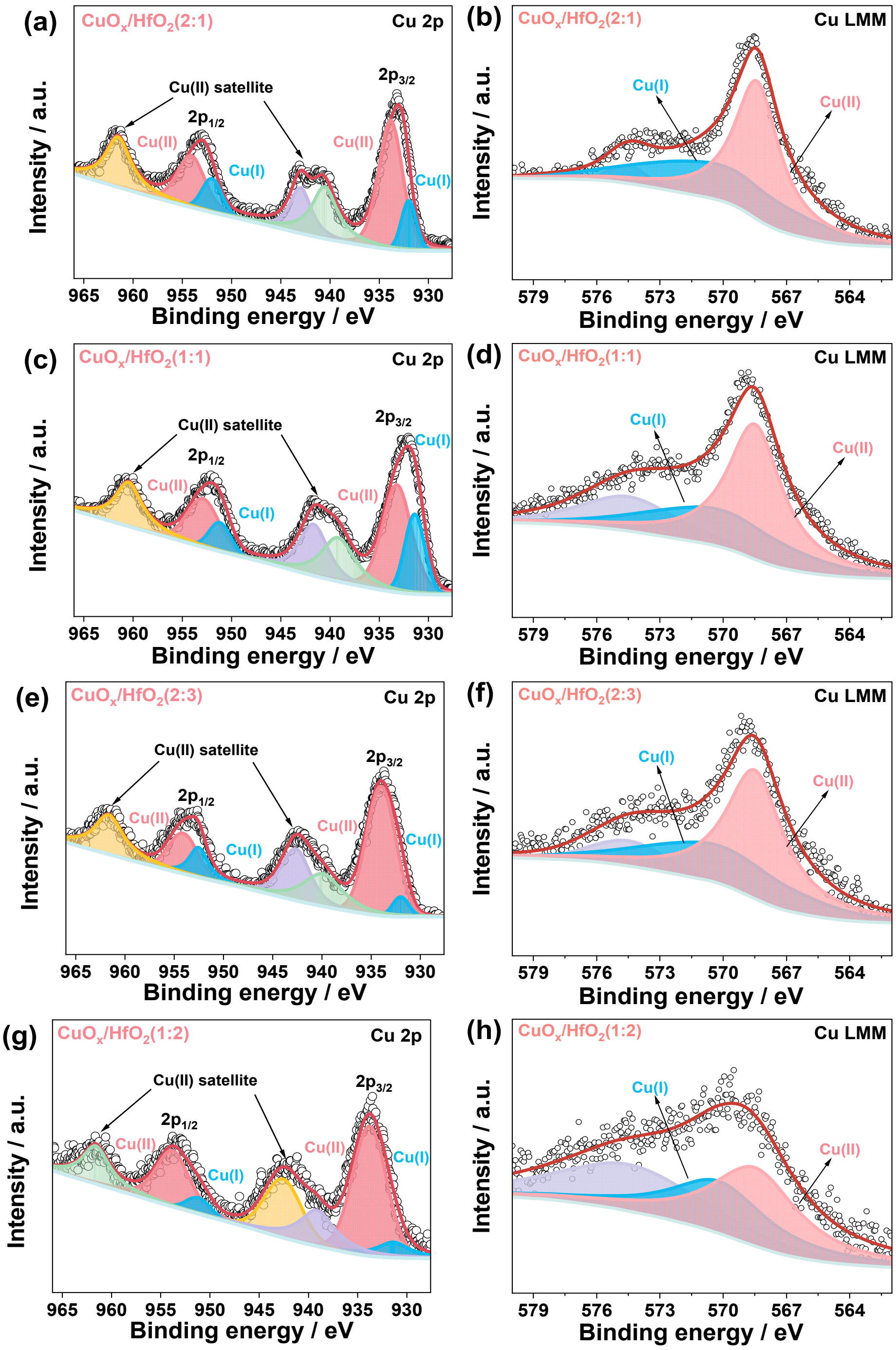

Fig. S3. Cu 2p XPS spectra for (a) $CuO_x/HfO_2(2:1)$, (c) $CuO_x/HfO_2(1:1)$, (e) $CuO_x/HfO_2(2:3)$, and (g) $CuO_x/HfO_2(1:2)$. Cu LMM spectra for (b) $CuO_x/HfO_2(2:1)$, (d) $CuO_x/HfO_2(1:1)$, (f) $CuO_x/HfO_2(2:3)$, and (h) $CuO_x/HfO_2(1:2)$.

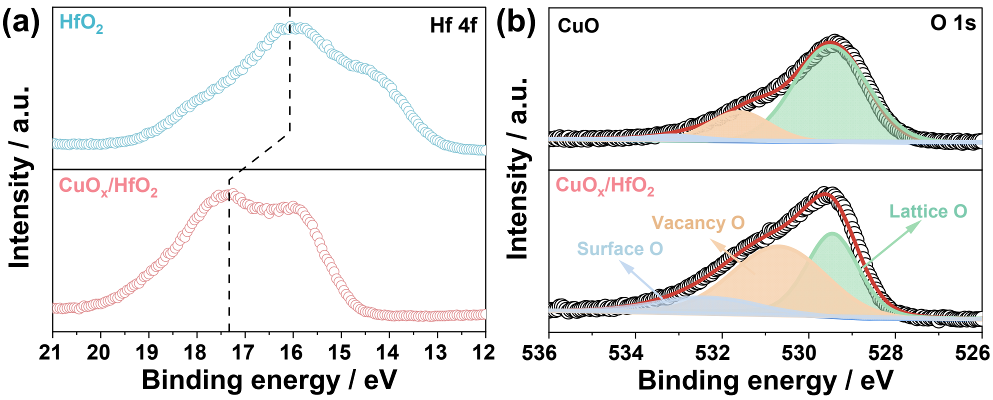

Fig. S4. (a) Hf 4f XPS spectra of CuO_x/HfO_2(3:2) and HfO_2. (b) O 1s XPS spectra of CuO and CuO_x/HfO_2(3:2).

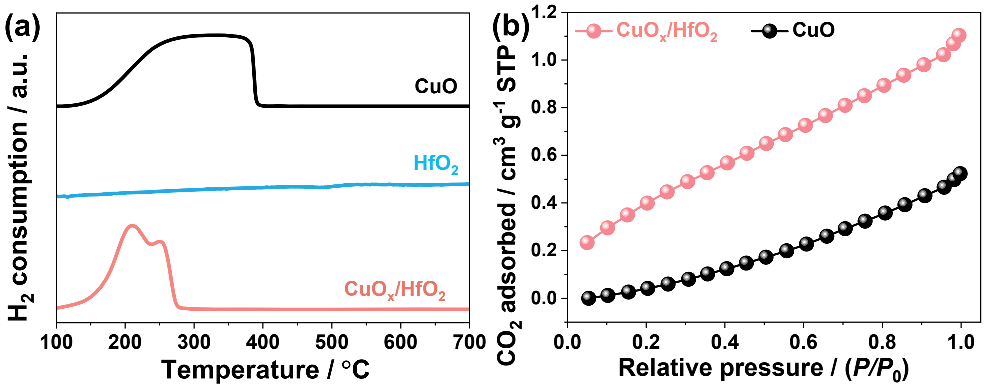

Fig. S5. (a) H_2-TPR profiles of CuO_x/HfO_2(3:2), CuO, and HfO_2. (b) CO_2 adsorption isotherms of CuO and CuO_x/HfO_2(3:2).

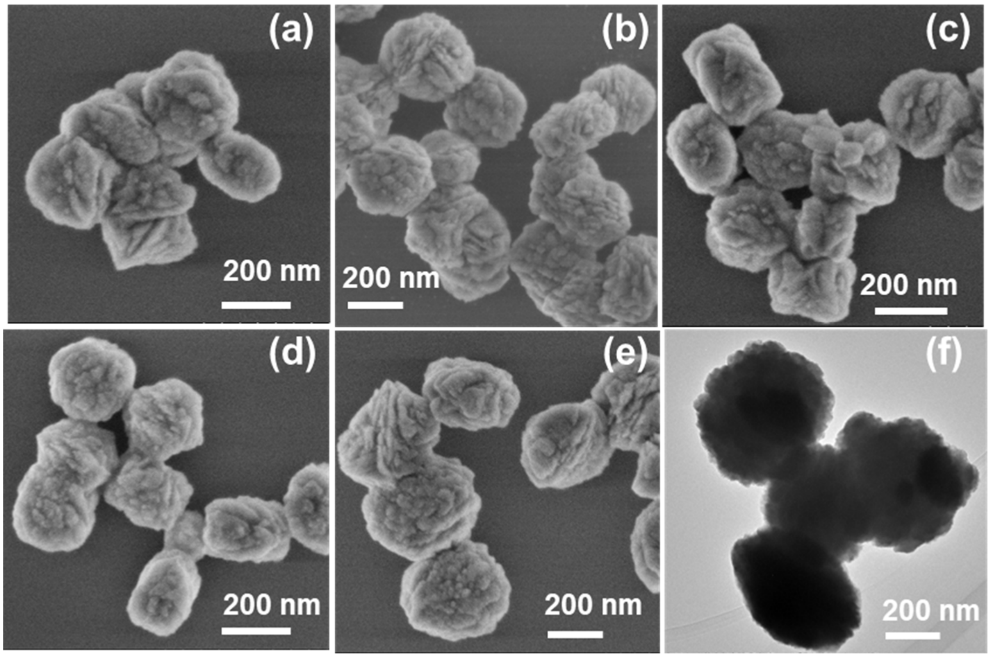

Fig. S6. SEM images of CuO_x/HfO_2 with a Cu-to-Hf molar ratio of (a) 2:1, (b) 3:2, (c) 1:1, (d) 2:3, (e) 1:2, and (f) TEM image of CuO_x/HfO_2 with a Cu-to-Hf molar ratio of 3:2.

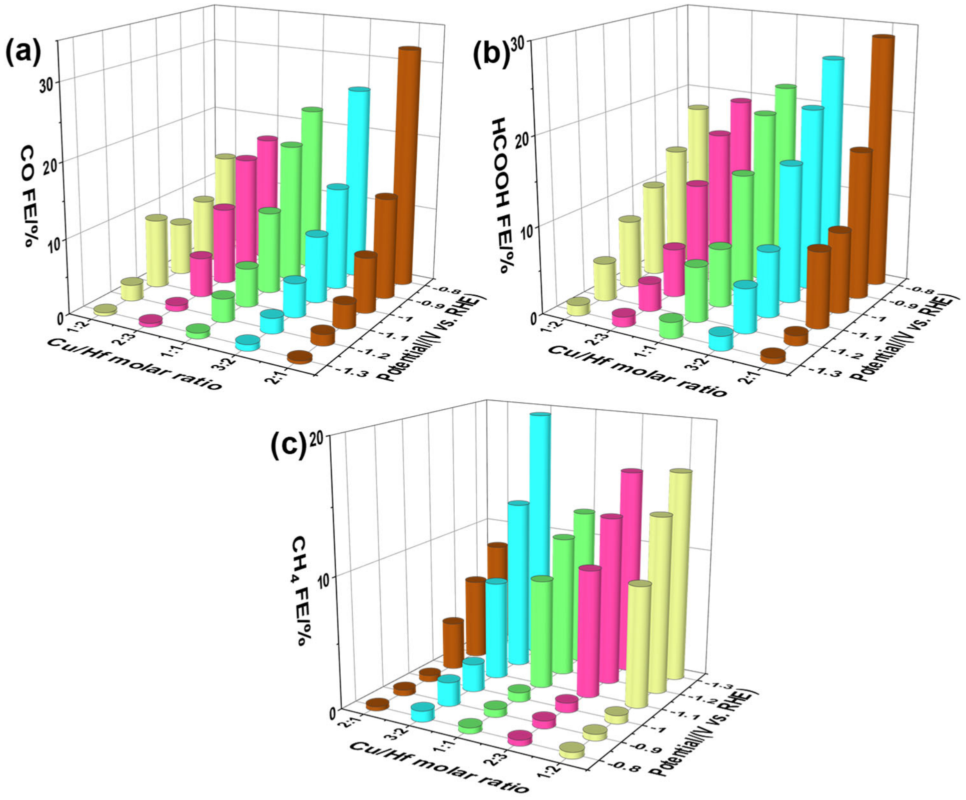

Fig. S7. FEs of (a) CO, (b) HCOOH, and (c) CH_4 for CuO_x/HfO_2 with various molar ratios at different applied potentials in 0.1 M $KHCO_3$.

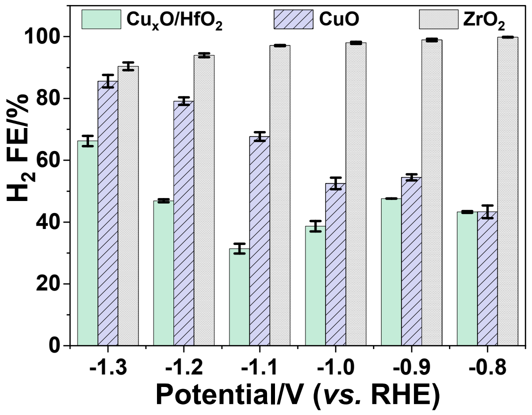

Fig. S8. H_2 FEs over CuO (striped column), HfO_2 (dotted column), and CuO_x/HfO_2(3:2) at distinct potentials.

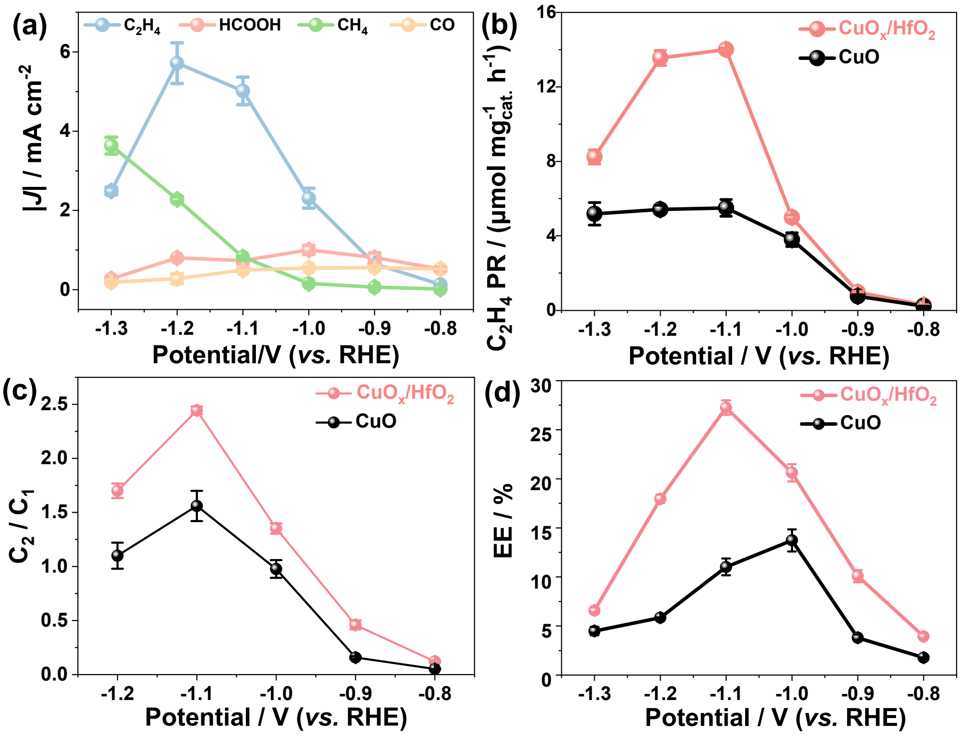

Fig. S9. (a) The absolute partial current density for different ECR products at distinct applied potentials over CuO_x/HfO_2(3:2). (b) C_2H_4 production rates, (c) C_2/C_1 product selectivity and (d) C_2H_4 EE on CuO and CuO_x/HfO_2(3:2) at varying voltages.

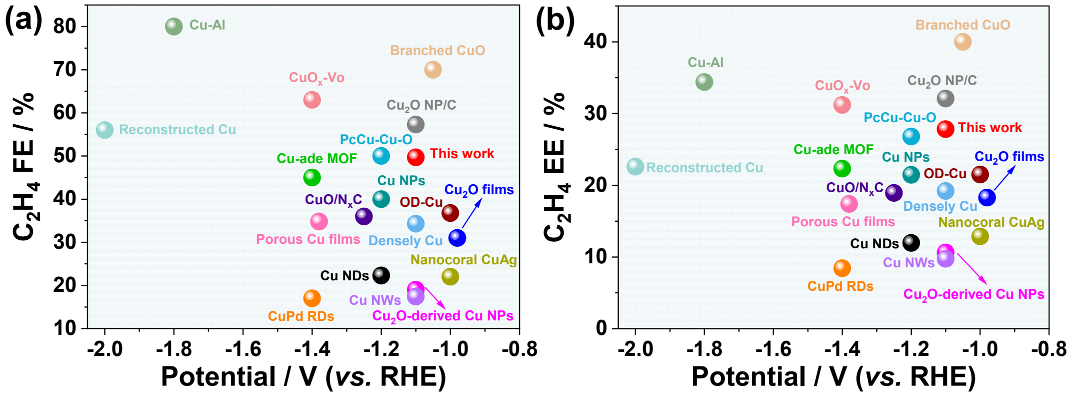

Fig. S10. (a) FEs and (b) EEs of C_2H_4 over CuO_x/HfO_2(3:2) and other recently reported Cu-based electrocatalysts in literature.

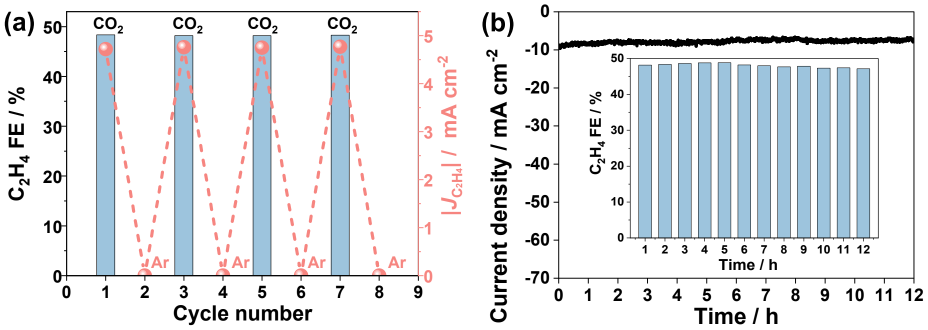

Fig. S11. (a) C_2H_4 FEs (bar) and corresponding absolute partial current densities (ball) over $CuO_x/HfO_2(3:2)$ during cycles with an interval of 1 h in CO_2- and Ar-saturated 0.1 M $KHCO_3$ at −1.1 V. (b) Current density versus electrolysis time over $CuO_x/HfO_2(3:2)$. The inset shows the respective C_2H_4 FE–time response.

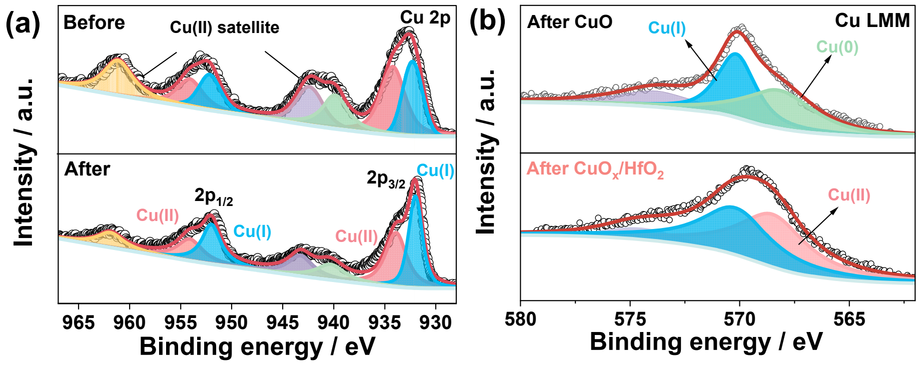

Fig. S12. (a) Cu 2p XPS spectra of CuO_x/HfO_2 before and after 1 h of electrolysis. (b) Cu LMM Auger XPS spectra of CuO_x/HfO_2 and CuO after CO_2 electrolysis.

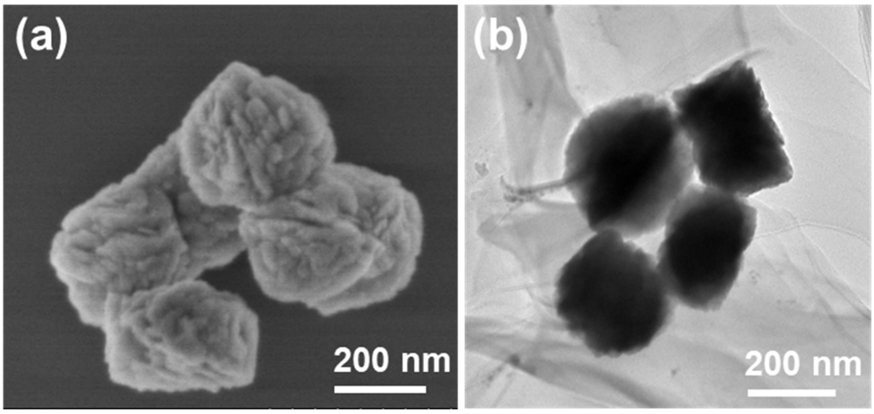

Fig. S13. (a) SEM and (b) TEM images of CuO_x/HfO_2 collected after 1 h of CO_2 electrolysis.

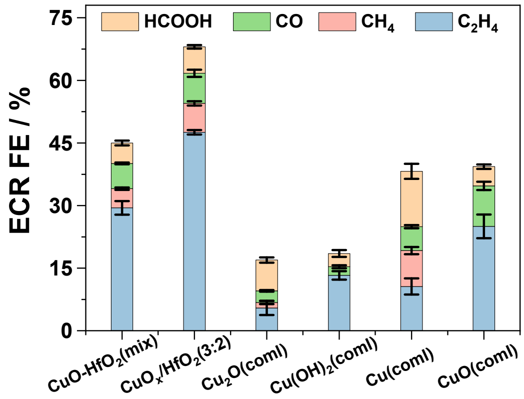

Fig. S14. C_2H_4 FE over CuO_x/HfO_2 catalysts with commercial (coml) Cu, Cu_2O, CuO, and $Cu(OH)_2$.

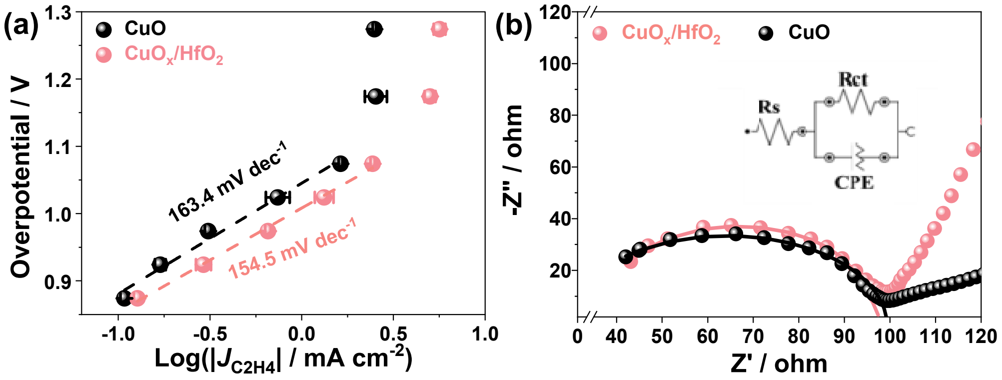

Fig. S15. (a) Tafel plots of the partial geometric current density for C_2H_4 production over CuO_x/HfO_2(3:2) and CuO. (b) Nyquist plots along with corresponding fitting curves for CuO and CuO_x/HfO_2(3:2).

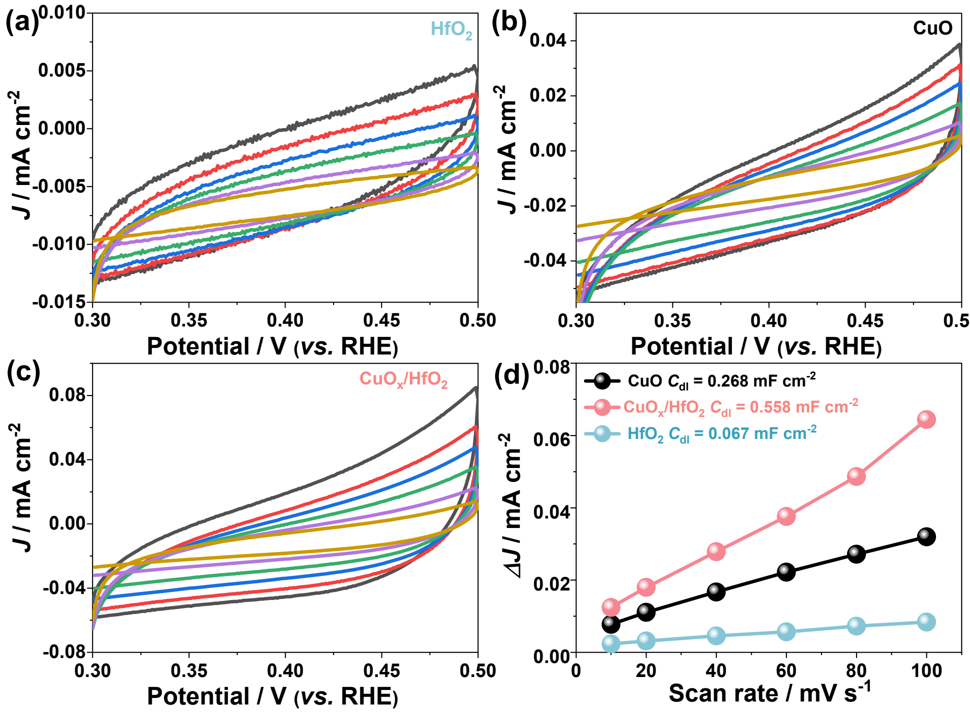

Fig. S16. The cyclic voltammetry results on (a) HfO$_2$, (b) CuO, and (c) CuO$_x$/HfO$_2$(3:2) at different scan rates (10, 20, 40, 60, 80, and 100 mV s^{-1}). (d) Charging current density differences plotted against scan rate.

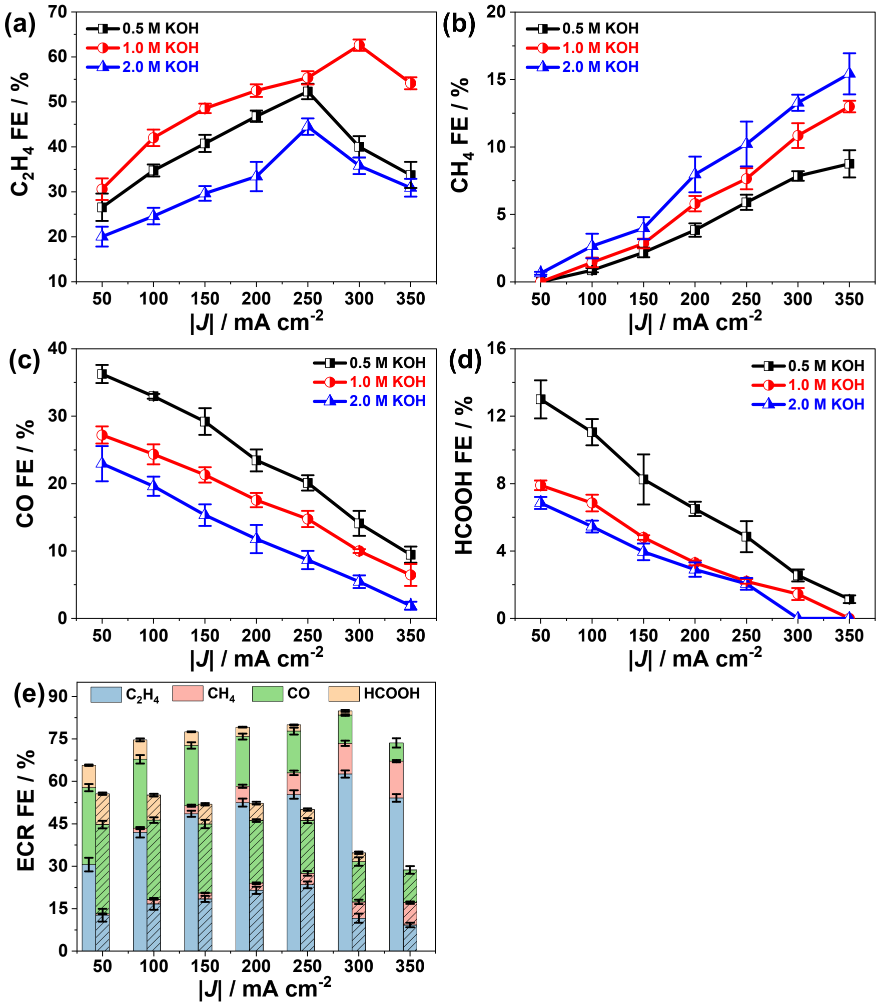

Fig. S17. FE of (a) C_2H_4, (b) CH_4, (c) CO, and (d) HCOOH versus current density on CuO_x/HfO_2(3:2) at different electrolyte concentrations. (e) ECR FEs of CuO_x/HfO_2(3:2) (left column) and bare CuO (right column) at geometric current densities from 50 to 350 mA cm^{-2} in a flow cell.

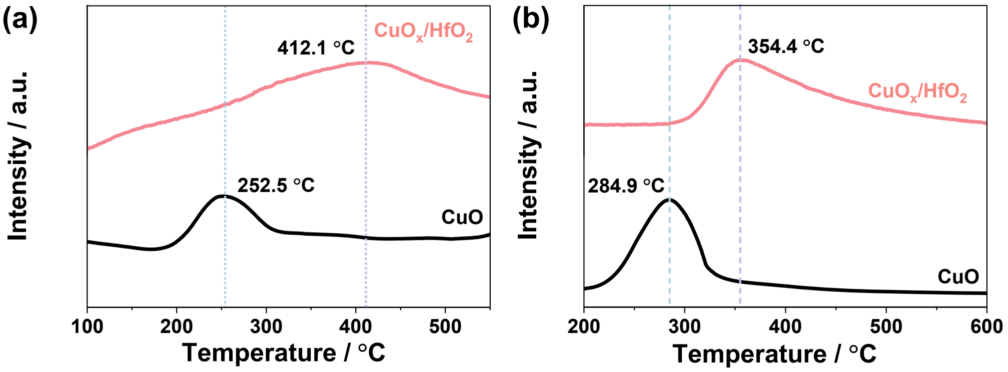

Fig. S18. (a) CO_2-TPD and (b) CO-TPD profiles for CuO and CuO_x/HfO_2(3:2).

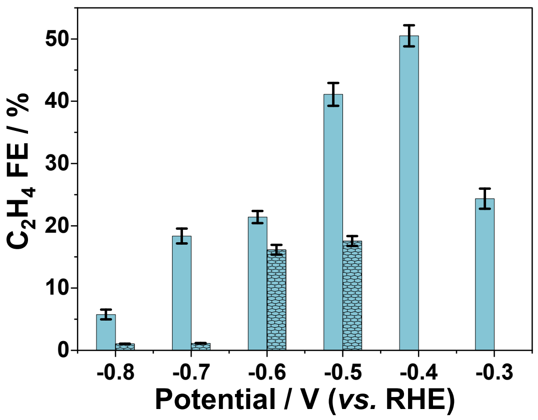

Fig. S19. FE for C_2H_4 formation via the electrochemical CO reduction over bare CuO and CuO_x/HfO_2(3:2) in 0.1 M KOH solutions saturated with CO at ambient temperature.

Table S1. The relative percentages of Cu^+ and Cu^{2+} in CuO_x/HfO_2 samples based on XPS estimations.

Catalyst	Nominal Cu-to-Hf molar ratio	Cu^+ surface fraction (%)	Cu^{2+} surface fraction (%)
CuO_x/HfO_2(2:1)	2	22.1	77.9
CuO_x/HfO_2(3:2)	1.5	43.6	56.4
CuO_x/HfO_2(1:1)	1	30.2	69.8
CuO_x/HfO_2(2:3)	0.67	18.1	81.9
CuO_x/HfO_2(1:2)	0.5	11.2	88.8

Table S2. Summary of C_2H_4 FE and EE of the CuO_x/HfO_2 and other newly reported Cu-based catalysts in H-cells.

Catalyst	Potential (V *vs.* RHE)	C_2H_4 FE (%)	C_2H_4 EE (%)	Ref.
CuO_x/HfO_2(3:2)	**–1.1**	**~50**	**27.3**	**This work**
Cu_2O films	–0.98	31	18.3	2
OD-Cu	–1	36.7	21.5	3
Nanocoral CuAg	–1	22	12.9	4
Branched CuO	–1.05	70	40	5
Cu meshes	–1.1	34.3	19.2	6
Cu_2O derived Cu NPs	–1.1	19	10.6	7
Cu NWs	–1.1	17.4	9.7	8

Cu_2O NP/C	−1.1	57.3	32.1	9
Cu NDs	−1.2	22.3	12	10
ERD Cu	−1.2	40	21.5	11
PcCu-Cu-O	−1.2	50	26.8	12
CuO/N_xC	−1.25	36	18.9	13
Porous Cu films	−1.38	34.8	17.4	14
Cu-ade MOF	−1.4	45	22.3	15
CuPd RDs	−1.4	17	8.4	16
CuO_x-Vo	−1.4	63	31.2	17
Cu-Al	−1.8	80	34.4	18
Reconstructed Cu	−2	56	22.6	19

Table S3. The ECR activity optimized by modulating the feeding sequence of the metal salt precursors.

Sample	Feeding sequence$_{\text{metal salt prescursors}}$	FE$_{C_2H_4}$ (%)
CuO_x-HfO_2(3:2)	Firstly: $Cu(Ac)_2 \cdot H_2O$ + NaOH Secondly: $HfCl_4$	24.2
CuO_x/HfO_2(3:2)	$Cu(Ac)_2 \cdot H_2O$ + $HfCl_4$ + NaOH	48.7
HfO_2-CuO(3:2)	Firstly: $HfCl_4$ + NaOH Secondly: $Cu(Ac)_2 \cdot H_2O$	27.8
CuO_x-HfO_2-CuO_x	Firstly: $Cu(Ac)_2 \cdot H_2O$ + NaOH Secondly: $HfCl_4$ Thirdly: $Cu(Ac)_2 \cdot H_2O$	21.6

Table S4. Summary of C_2H_4 FE of CuO_x/HfO_2 and other recently reported Cu-based catalysts in flow cells.

Catalyst	C_2H_4 FE (%)	$\lvert J \rvert$ (mA cm^{-2})	Ref.
CuO_x/HfO_2	**62.6**	**300**	**This work**
Cu_4O_3-rich catalyst	40	400	20
ERD Cu	36	160	21
Cu nanoparticles	46	200	22
Cu	45.5	67.4	23
WCO-Cu GDE	30	150	24

Cu/ZnO tandem CL	40	600	25
Cu	50	>100	26
Reconstructed Cu	84	336	19
Cu nanocrystals	44	260	27
CuAg wire	55	311	28
Ce-doped Cu nanoparticles	53	150	29
Cu/molecule	72	320	30

References

1 A. Tatin, C. Comminges, B. Kokoh, C. Costentin, M. Robert and J. -M. Savéant, *Proc. Natl. Acad. Sci. U. S. A.*, 2016, **113**, 5526–5529.

2 A. D. Handoko, W. O. Cheng, H. Yun, G. L. Zheng and B. S. Yeo, *J. Phy. Chem. C*, 2016, **120**, 20058–20067.

3 J. Liu, J. Fu, Y. Zhou, W. Zhu, L.-P. Jiang and Y. Lin, *Nano Let.*, 2020, **20**, 4823–4828.

4 Z. Y. Chang, S. J. Huo, W. Zhang, J. H. Fang and H. L. Wang, *J. Phys. Chem. C*, 2017, **121**,11368–11379.

5 J. Kim, W. Choi, J.W. Park, C. Kim, M. Kim and H. Song, *J. Am. Chem. Soc.*, 2019, **141**, 6986–6994.

6 M. Rahaman, A. Dutta, A. Zanetti and P. Broekmann, *ACS Catal.*, 2017, **7**, 7946–7956.

7 R. Kas, R. Kortlever, A. Milbrat, M. Koper, G. Mul and J. Baltrusaitis, *Phy. Chem. Chem. Phy.*, 2014, **16**, 12194–12201.

8 M. Ma, K. Djanashvili and W. A. Smith, *Angew. Chem. Int. Ed.*, 2016, **55**, 6680–6684.

9 H. Jung, S. Y. Lee, C. W. Lee, M. K. Cho, D. H. Won, C. Kim, H. -S. Oh, B. K. Min and Y. J. Hwang, *J. Am. Chem. Soc.*, 2019, **141**, 4624–4633.

10 M. Wu, C. Zhu, K. Wang, G. Li, X. Dong, Y. Song, J. Xue, W. Chen, W. Wei and Y. Sun, *ACS App. Mater. Inter.*, 2020, **12**, 11562–11569.

11 P. D. Luna, R. Quintero-Bermudez, C. T. Dinh, M. B. Ross, O. S. Bushuyev, P. Todorovi, T. Regier, S. O. Kelley, P. Yang and E. H. Sargent, *Nat. Catal.*, 2018, **1**, 103–110.

12 X. F. Qiu, H. L. Zhu, J. R. Huang, P. Q. Liao and X. M. Chen, *J. Am. Chem. Soc.*, 2021, **143**, 7242–7246.

13 H. J. Yang, H. Yang, Y. H. Hong, P. Y. Zhang, T. Wang, L. N. Chen, F. Y. Zhang, Q. H. Wu, N. Tian and Z. Y. Zhou, *ChemSusChem*, 2018, **11**, 881–887.

14 M. Padilla, O. Baturina, J. P. Gordon, K. Artyushkova, P. Atanassov and A. Serov, *J. CO_2 Util.*, 2017, **19**, 137–145.

15 F. Yang, A. Chen, P. L. Deng, Y. Zhou, Z. Shahid, H. Liu and B. Y. Xia, *Chem. Sci.*, 2019, **10**, 7975–7981.

16 Z. Wang, G. Yang, Z. Zhang, M. Jin and Y. Yin, *ACS Nano*, 2016, **10**, 4559–4564.

17 Y. Liu, X. Fan, A. Nayak, Y. Wang and T. J. Meyer, *Proc. Natl. Acad. Sci. U. S. A.*, 2019, **116**, 26353–26358.

18 H. Bao, Y. Qiu, X. Peng, J. A. Wang and X. Sun, *Nat. Commun.*, 2021, **12**, 238.

19 M. G. Kibria, C. Dinh, A. Seifitokaldani, P. D. Luna, T. Burdyny, R. Quintero-Bermudez, M. B. Ross, O. S. Bushuyev, F. Arquer and P. Yang, *Adv. Mater.*, 2018, **30**, 1804867.

20 N. Martic, C. Reller, C. Macauley, M. Löffler, B. Schmid, D. Reinisch, E. Volkova, A. Maltenberger, A. Rucki, K. Mayrhofer and G. Schmid, *Adv. Energy Mater.*, 2019, **9**, 1901228.

21 P. De Luna, R. Quintero-Bermudez, C. Dinh, M. Ross, O. Bushuyev, P. Todorovic, T. Regier, S. Kelley, P. Yang and E. Sargent, *Nat. Catal.,* 2018, **1**, 103–110.

22 S. C. Ma, M. Sadakiyo, R. Luo, M. He, M. Yamauchi and P. Kenis, *J. Power Sources*, 2016, **301**, 219–228.

23 S. Perry, S. Gateman, R. Malpass-Evans, N. McKeown, M. Wegener, P. Nazarovs, J. Mauzeroll, L. Wang and C. Ponce de Leon, *Chemosphere*, 2020, **248**, 125993.

24 J. Zhang and W. Luo, *J. Mater. Chem. A*, 2019, **7**, 26285.

25 T. Zhang, Z. Li, J. Zhang and J. Wu, *J. Catal.*, 2020, **387**, 163–169.

26 C. M. Gabardo, C. O'Brien, J. Edwards, C. McCallum, Y. Xu, C. Dinh, J. Li, E. H. Sargent and D. Sinton, *Joule*, 2019, **3**, 2777–2791.

27 H. S. Jeon, J. Timoshenko, C. Rettenmaier, A. Herzog, A. Yoon, S. W. Chee, S. Oener, U. Hejral, F. T. Haase and B. Roldan Cuenya, *J. Am. Chem. Soc.*, 2021, **143**, 7578–7587.

28 T. T. H. Hoang, S. Verma, S. Ma, T. T. Fister, J. Timoshenko, A. I. Frenkel, P. J. A. Kenis and A. A. Gewirth, *J. Am. Chem. Soc.*, 2018, **140**, 579–5797.

29 J. Shan, Y. Shi, H. Li, Z. Chen, C. Sun, Y. Shuai and Z. Wang, *Chem. Eng. J.*, 2022, **433**, 133769.

30 F. Li, A. Thevenon, A. Rosas-Hernández, Z. Wang, Y. Li, C. M. Gabardo, A. Ozden, C. T. Dinh, J. Li, Y. Wang, J. P. Edwards, Y. Xu, C. McCallum, L. Tao, Z.-Q. Liang, M. Luo, X. Wang, H. Li, C. P. O'Brien, C.-S. Tan, D.-H. Nam, R. Quintero-Bermudez, T.-T. Zhuang, Y. C. Li, Z. Han, R. D. Britt, D. Sinton, T. Agapie, J. C. Peters and E. H.

Sargent, *Nature*, 2020, **577**, 509–513.